

https://doi.org/10.1070/QEL17560

Reconstruction of fluorophore concentration distribution in diffuse fluorescence tomography based on Tikhonov regularisation and nonnegativity condition

I.I. Fiks, I.V. Turchin

Abstract. **We propose to solve the inverse problem of diffuse fluorescence tomography (DFT) – reconstruction of the spatial distribution of the fluorophore in biological tissues – by a method based on Tikhonov regularisation with the nonnegativity condition (TRNC) of the reconstructed components of the solution vector. Model experiments on a biotissue phantom demonstrate that the TRNC method allows for a more accurate reconstruction of the distribution of the fluorophore concentration, and is also more stable in comparison with the known algorithms used in DFT, such as ART, SMART, NNLS, etc.**

Keywords: *diffuse fluorescence tomography, Tikhonov regularisation, nonnegativity condition for the solution vector, fluorescence molecular imaging.*

1. Introduction

Fluorescence imaging, with its high molecular sensitivity, is a widespread method for studying biological objects of various sizes, from submicrons to a few centimetres [1]. The methods of fluorescence microscopy [2] and nanoscopy [3] make it possible to visualise subcellular structures with high spatial resolution from submicrons for laser scanning microscopy systems to several nanometres in superresolution microscopy. However, the depth of such studies is limited by the photon mean free path in tissue, which is about 100 μm. When studying objects on larger scales exceeding one transport mean free path (about 1 mm in biological tissues), the effects of multiple scattering become more significant, resulting in blurring the probe beam, which does not allow micron-scale spatial resolution to be achieved. Nevertheless, fluorescence imaging of living objects on scales of several millimetres and more is an equally urgent problem and is used both in clinical diagnostics and in laboratory studies on animals. For example, fluorescence imaging using contrast agents makes it possible to assess tumour boundaries with better accuracy during organ-preserving surgeries [4, 5], as well as to visualise the circulatory and lymphatic systems [6]. In studies on laboratory animals, which are carried out in the field of experimental oncology, fluorescently labelled tumour lines [7] are used to determine the size of the primary tumour and the presence of metastases [8], to study complex molecular processes such as apoptosis [9], to determine the pH level in a tumour [10], etc. With an increase in the depth of a fluorescently labelled inclusion, e.g., an experimental tumour expressing fluorescent proteins, the blurring of its fluorescent response on the surface of an object increases, leading to larger errors in determining its true size and localisation.

Various instrumental approaches are used to reduce the blurring effects of fluorescent objects associated with light scattering. The use of raster scanning of an object with a narrow mono-directional excitation source (raster-scan illumination) synchronously with a detector (raster-scan detection), which registers fluorescence from the same area, makes it possible to narrow the sensitivity area at each position of the source and detector [11]. In this case, systems with a transillumination configuration, in contrast to a reflection one, are less sensitive to the depth position of the fluorescent inclusion [12–14].

The techniques listed above allow one to decrease the blurring effect in two-dimensional fluorescent images in comparison with standard broad beam illumination with wide-field camera detection, but they do not provide full three-dimensional information about the distribution of the fluorophore in the object of study.

The problem of three-dimensional reconstruction of the spatial distribution of the fluorophore concentration is solved by the method of diffuse fluorescence tomography (DFT) [15], based on obtaining a set of projections of the object irradiated by a source that excites fluorescence, and registering the emission with subsequent reconstruction of the distribution of the fluorophore in tissue by mathematical methods. This approach usually uses plane or cylindrical scanning geometries [16]. There is also a modification of DFT based on the use of structured illumination with different spatial frequencies [17].

Since multiply scattered photons are registered in the DFT, there are a number of factors that limit the accuracy of the solution to the inverse problem. They include high sensitivity to boundary conditions, limitations of well-known analytical models, e.g., the diffusion approximation of the radiation transfer equation, high sensitivity to noise, both instrumental and associated with an autofluorescence background. All this leads to the ill-posedness of the inverse problem and, as a consequence, to high requirements for both the instrumental part and the reconstruction algorithms, which are being permanently improved.

Since the propagation of optical radiation in biological tissues is described by the radiative transfer equation (RTE) [18], which has an integro-differential form, it is not possible to obtain an analytical expression for the spatial distribution of the fluorophore concentration, and various numerical

I.I. Fiks, I.V. Turchin Institute of Applied Physics, Russian Academy of Sciences, ul. Ulyanova 46, 603950 Nizhny Novgorod, Russia; e-mail: ilya340@mail.ru

Received 26 March 2021
Kvantovaya Elektronika **51** (5) 400–407 (2021)
Translated by V.L. Derbov

algorithms are used to solve the DFT problem. In the overwhelming majority of cases, the concentration of the fluorophore can be considered relatively small in the sense that the contribution to the absorption coefficient of the probe radiation associated with the presence of the fluorophore is much less than the intrinsic absorption coefficient of biological tissues. In this case, the DFT problem is reduced to solving the Fredholm equation of the first kind [19], which, in turn, is reduced to a system of linear equations.

Unlike reconstruction in X-ray and magnetic resonance tomography, the matrix of the DFT system is nonsparse; moreover, due to the singularity of the Fredholm equation kernel, the system is poorly conditioned [20]. This means that small deviations in the experimental data lead to large changes in the reconstruction results. The elements of the inverted matrix are also calculated with some error, which is due to the imperfection of the applied model of light propagation in tissues. To improve the accuracy of reconstruction in DFT, models of radiation propagation in randomly inhomogeneous media are used, which are closer to reality than the traditionally used diffusion approximation of RTE, e.g., Monte Carlo simulation [21] and hybrid analytical models [22]. To take into account the boundary conditions in the radiation propagation model correctly, the anatomical structure of the object, obtained using X-ray or magnetic resonance tomography, is used [23–25]. It is also important to take into account the autofluorescence background in the registered signal, which is possible using multispectral measurements [26, 27]. The number of measurements (projections) at different positions of the radiation source and detector should significantly exceed the number of reconstructed elements (voxels).

In addition to the approaches listed above, the algorithm for solving a system of linear equations itself plays an equally important role in DFT. In algorithms, it is important to maximise the use of *a priori* information about the reconstructed vector, for example, about the location and shape of the fluorescent inclusion. The 'natural' *a priori* knowledge in DFT is the nonnegativity of the fluorophore concentration. Earlier it was shown that the use of this condition significantly increases the condition number of the inverse problem [28]. Nevertheless, despite the wide variety of algorithms used in DFT, only a few of them correctly use this condition. Due to the ill-posedness of the inverse DFT problem, it is also reasonable to use regularisation procedures in algorithms.

The classical method used in DFT is the algebraic reconstruction technique (ART) [29–31], which uses zeroing of negative components of the current vector at each iteration step, which is incorrect from the mathematical point of view due to the convergence uncertainty of such an algorithm. A modification of this algorithm, the simultaneous multiplicative algebraic reconstruction technique (SMART) [32], correctly uses the nonnegativity condition, but has a very low convergence rate. Another method, the nonnegative least squares (NNLS) method [33], which correctly takes into account the nonnegativity condition, does not have any regularisation procedures, which leads to the solution instability.

The gold standard for solving ill-conditioned systems of linear equations is Tikhonov regularisation (TR) [20], which belongs to L2-regularisation methods; however, this method does not allow obtaining a nonnegative solution. L1-regularisation methods, such as LASSO [34], adaptive group orthogonal matching pursuit [35], kernel method [36], and sparsity adaptive correntropy matching pursuit method [37], have a significant advantage over TR, namely, the resulting solution is less 'blurred' compared to a fluorescent object, which makes it possible to determine its size more accurately. However, this approach, like TR, does not consider the nonnegativity condition.

Thus, in the methods listed above, either regularisation procedures, or the nonnegativity condition are not used or used incorrectly.

It should also be noted that a new approach to DFT based on machine learning methods, in particular on neural networks, showed a better result compared to the results of existing reconstruction methods [38]. However, this approach requires the unification of the initial data for solving a specific DFT problem, in which the positions of sources and detectors, the parameters of the partitioning grid of the original object, etc., must be rigidly specified. Otherwise, the task of the neural network training becomes very complicated.

To solve the DFT problem it is proposed here to use the TR-based algorithm, previously developed by us, that takes into account the nonnegativity of the reconstructed components (TRNC) [28]. The nonnegativity conditions in this method are introduced inside the iterative procedure, like in the SMART method, and so it does not artificially zero out the current vector components, as in ART and NNLS.

This paper describes an iterative procedure for the TRNC algorithm and compares the results of reconstructing the spatial distribution of a fluorophore in a model object (biological tissue phantom) with the results of ART, SMART, and TR algorithms, as well as matrix inversion (MI) and NNLS algorithms. The biological tissue phantom was scanned using an experimental DFT setup developed at the Institute of Applied Physics of the Russian Academy of Sciences (Nizhny Novgorod, Russia) and intended for the study of small laboratory animals.

2. Materials and methods

2.1. Statement of the DFT inverse problem

The spatial distribution of the fluorophore concentration in the tissue $\Phi(\boldsymbol{r}_0)$, where $\boldsymbol{r}_0$ is a set of points belonging to the tissue volume V under study, can be found using the data on the intensities of the fluorescence signal $P_{\text{exp}}(\boldsymbol{r}_\text{s}, \boldsymbol{r}_\text{d})$ registered for different locations of the radiation source $\boldsymbol{r}_\text{s}$ and detector $\boldsymbol{r}_\text{d}$. If the absorption coefficient of the fluorophore distributed in the tissue is much less than the absorption coefficient of the tissue itself, the problem can be considered linear. The function $\Phi(\boldsymbol{r}_0)$ is sought among the set of values that satisfy the condition $\Phi(\boldsymbol{r}_0) \geqslant 0, \forall \boldsymbol{r}_0 \in V$, as a solution to the Fredholm integral equation of the first kind [39]

$$P_{\text{exp}}(\boldsymbol{r}_\text{s}, \boldsymbol{r}_\text{d}) = \int_V \Phi(\boldsymbol{r}_0) F(\boldsymbol{r}_\text{s}, \boldsymbol{r}_0, \boldsymbol{r}_\text{d}) \, \mathrm{d}\boldsymbol{r}_0, \tag{1}$$

where $F(\boldsymbol{r}_\text{s}, \boldsymbol{r}_0, \boldsymbol{r}_\text{d})$ is the point spread function determined by the optical properties of a turbid medium (scattering and absorption coefficients), boundary conditions, characteristics of the source and detector, as well as the brightness of the fluorophore. Since F and P_{exp} include many multiplicative parameters (source power, spectral sensitivity of the detector, quantum yield and absorption coefficient of the fluorophore, refractive index of the object under study, etc.), which are difficult to measure, the distribution function of the fluorophore is determined up to an arbitrary factor.

To solve the integral equation (1), the original volume V is divided into N disjoint voxels. There are various methods of division; in particular, tetragonal computational grids with a variable step can be used for an arbitrary surface. However, to demonstrate the operation of the proposed TRNC algorithm, we will use a simplified model, namely, a medium in the form of a rectangular parallelepiped with equidistant division along the$x$, y, and z axes into N_x, N_y and N_z parts with corresponding steps dx, dy and dz. Then Eqn (1) can be represented in the form of a system of linear equations of dimension $M \times N$, where $N = N_x N_y N_z$, and M is the number of measurements with different positions of the source $\boldsymbol{r}_s$and detector $\boldsymbol{r}_d$:

$$\boldsymbol{A}\boldsymbol{v} = \boldsymbol{p}. \tag{2}$$

Here $\boldsymbol{A}$ is an $M \times N$ matrix of nonnegative real numbers, which characterises the point spread function in Eqn (1); $\boldsymbol{p}$ is a vector of real numbers of dimension M characterising the results of measurements of the fluorescence intensity; and $\boldsymbol{v}$ is the sought vector of dimension N, which describes the distribution of the fluorophore concentration. The vector $\boldsymbol{v}$ is sought in the class of nonnegative numbers: $v_j \geqslant 0, j = 1, \ldots, N$.

2.2. Iterative procedure of the TRNC algorithm

The iterative TRNC algorithm is described in [28]. In this approach, in contrast to other reconstruction methods, conditional optimisation is changed for unconditional one and the vector $\boldsymbol{v}$ reconstructed from Eqn (2) is represented as $\boldsymbol{v} = \left\{v_j = u_j^2,\ j = \overline{1,N},\ u_j \in R\right\}$ or, in matrix-vector form,

$$\boldsymbol{v} = \boldsymbol{D}(\boldsymbol{u})\boldsymbol{u}, \tag{3}$$

where $\boldsymbol{D}(\boldsymbol{u})$ is the diagonal matrix of the vector $\boldsymbol{u}$. Then the iterative procedure can be written in the form:

$$\boldsymbol{u}_{k+1} = \omega\boldsymbol{u}_k + (1-\omega)(\boldsymbol{D}(\boldsymbol{u}_k)\boldsymbol{A}^{\mathrm{T}}\boldsymbol{A}\boldsymbol{D}(\boldsymbol{u}_k) + \alpha\boldsymbol{E})^{-1}\boldsymbol{D}(\boldsymbol{u}_k)\boldsymbol{A}^{\mathrm{T}}\boldsymbol{p}, \tag{4}$$

where $\boldsymbol{E}$ is the identity matrix; $0 < \omega < 1$ is the relaxation parameter; α is the regularisation parameter; and k is the iteration number. The convergence and stability of this algorithm are also described in [28].

2.3. Experimental setup for DFT

The model experiment was carried out using the DFT setup developed at the Institute of Applied Physics of RAS. A schematic of the setup is shown in Fig. 1. It is based on the plane geometry of scanning the object under study by a laser beam that excites fluorescence in the object. The setup is designed for fluorescence studies in laboratory animals; red fluorescent proteins are used as a contrast agent. Most red fluorescent proteins (DsRed, DsRed2, TurboRFP, etc.) are efficiently excited by laser radiation with λ_{ex} = 532 nm. Radiation of an ATS-53-250 laser (CJSC 'Semiconductor Devices', Russia) at λ = 532 nm is delivered to the object of study using a multimode fibre and a collimating lens. At the research object, the radiation power is 20 mW, the beam diameter is 2 mm. The collimator lens is scanned in two coordinates using mechanical drives in the XY plane perpendicular to the direction Z of the probe beam propagation.

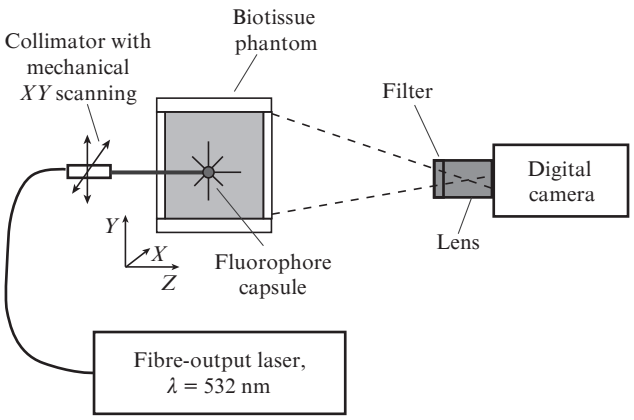

Figure 1. Schematic diagram of the DFT setup with plane geometry of transillumination scanning developed at the Institute of Applied Physics of RAS.

The system of scanning by the radiation source is similar to that used in the previously developed DFT setup [39]. The registration of fluorescence images is carried out at each position of the collimator lens in the transillumination configuration using a highly sensitive cooled digital camera ORCA II BT 512 (Hamamatsu Co., Japan), an S617/73m optical filter (Chroma Technology Co., USA), and an objective lens. The scanning and registering of fluorescence images are automated. The scanning step and the number of scanning points along the XY coordinates are set using the automation program developed by us.

2.4. Biotissue phantom

The biotissue phantom, on which the model experiment was carried out, is a quartz cell measuring 36 mm × 18 mm × 18 mm along the XYZ axes and containing a solution of intralipid and ink and a capsule with a DsRed2 fluorophore (Bach Institute of Biochemistry, RAS). The absorption coefficient μ_a and the reduced scattering coefficient μ_{sc}' for this solution at the excitation wavelength λ_{ex} = 532 nm are 0.2 and 2.7 cm^{-1}, respectively; at the centre fluorescence wavelength λ_{em} = 620 nm they are 0.05 and 1.8 cm^{-1}.

A glass spherical capsule with an inner diameter of 2 mm is placed in the cuvette, containing a solution of the fluorescent protein DsRed2 in a buffer medium to equalise the scattering and absorption of the environment and the fluorescent object.

As follows from the above values, the transport mean free path in a biotissue phantom $1/\mu_{sc}'$ is 4–6 mm, which is much less than the thickness of the cuvette (18 mm) and the depth of the capsule along the Z axis located near the cuvette centre. This means that the propagation of light in the biological tissue phantom is diffuse, except a small (less than 4 mm) region near the cuvette wall at the point of the probing beam incidence. Thus, to describe the optical field near the capsule, the reduced incident intensity component can be neglected.

2.5. Comparison of the efficiencies of TRNC and other reconstruction algorithms

To compare the efficiencies of the proposed TRNC algorithm and the standard ART, SMART, NNLS, TR and MI meth-

ods, iterative procedures that implement these methods were written in Matlab.

The results of measuring the fluorescence intensity obtained during the scanning of the biological tissue phantom are the data for the vector $\boldsymbol{p}$ in the system of linear equations (2). The matrix $\boldsymbol{A}$ is calculated using the RTE in hybrid approximation [22] with the scattering and absorption coefficients of the biological tissue phantom given in Section 2.4 and the coordinates of the sources and detectors specified in the scanning algorithm.

Note that all of the above methods, except MI, are applicable to systems with nonsquare matrices, and for reconstruction the MI method is applied to the system $\boldsymbol{A}^{\mathrm{T}}\boldsymbol{A}\boldsymbol{v} = \boldsymbol{A}^{\mathrm{T}}\boldsymbol{p}$, which is a system with a square matrix.

The iterative procedure of each algorithm stops when the average relative difference of adjacent iterations of the solution vector becomes less than 10^{-3}. A decrease in this threshold leads to a significant increase in the time of the iterative procedure.

The efficiency of the algorithm is estimated by the degree of closeness of the reconstructed fluorophore distribution to the original one, accurate to a constant factor. Another criterion for the efficiency of the reconstruction algorithm is its stability, which is estimated based on the solutions of a system of linear equations with a perturbed right-hand side

$$\boldsymbol{A}\boldsymbol{v} = \boldsymbol{p} + \Delta\boldsymbol{p}, \tag{5}$$

where $\Delta\boldsymbol{p}$ is a perturbation vector of the right-hand side, whose components obey the Rayleigh distribution. The results of solving Eqn (5) are compared with the initial distribution of the fluorophore at various relative perturbations $\delta p = \|\Delta\boldsymbol{p}\|_2/\|\boldsymbol{p}\|_2$, taking values $\delta p = 0.15$, 0.25, 0.35, and 0.75. Operation $\|\ldots\|_2$ means calculating the quadratic norm of a vector.

3. Results and discussion

3.1. Results of scanning the biological tissue phantom

Twenty-one fluorescent images of the biological tissue phantom were obtained using the DFT setup at 3×7 different X and Y positions of the radiation source with a step of 6 and 2 mm, respectively. Two images were removed from the original data set because of the low overall signal level. Thus, to reconstruct the distribution of the fluorophore, 19 images were selected, obtained at different positions of the source (Fig. 2g). In the original fluorescence images obtained with a digital camera, the uninformative part was cut off, including the regions beyond the biological tissue phantom, and the informative part of the image was compressed to 46×22 pixels (as a result of averaging over neighbouring pixels).

As seen from Fig. 2, the size of the fluorescence response is several times larger than the initial size of the fluorescent capsule (2 mm) due to scattering effects. In addition, it follows from Fig. 2 that the shape of the fluorescence response does not change when the radiation source is moved, but the overall level of the fluorescent signal changes, which is also associated with the diffuse nature of light propagation in turbid media.

3.2. Reconstruction of the fluorophore distribution

The number of columns of the matrix $\boldsymbol{A}$ in Eqn (2) is $M = 19 \times 46 \times 22$, which corresponds to the number of independent measurements at 19 different positions of the radiation source and 46×22 positions of the detecting elements. The volume to be reconstructed is divided into $N = 36 \times 18 \times 18$ voxels with a step of 1 mm. Thus, the system of linear equations (2) for the above model experiment is overdetermined and has the size: $N = 11664$ and $M = 19228$.

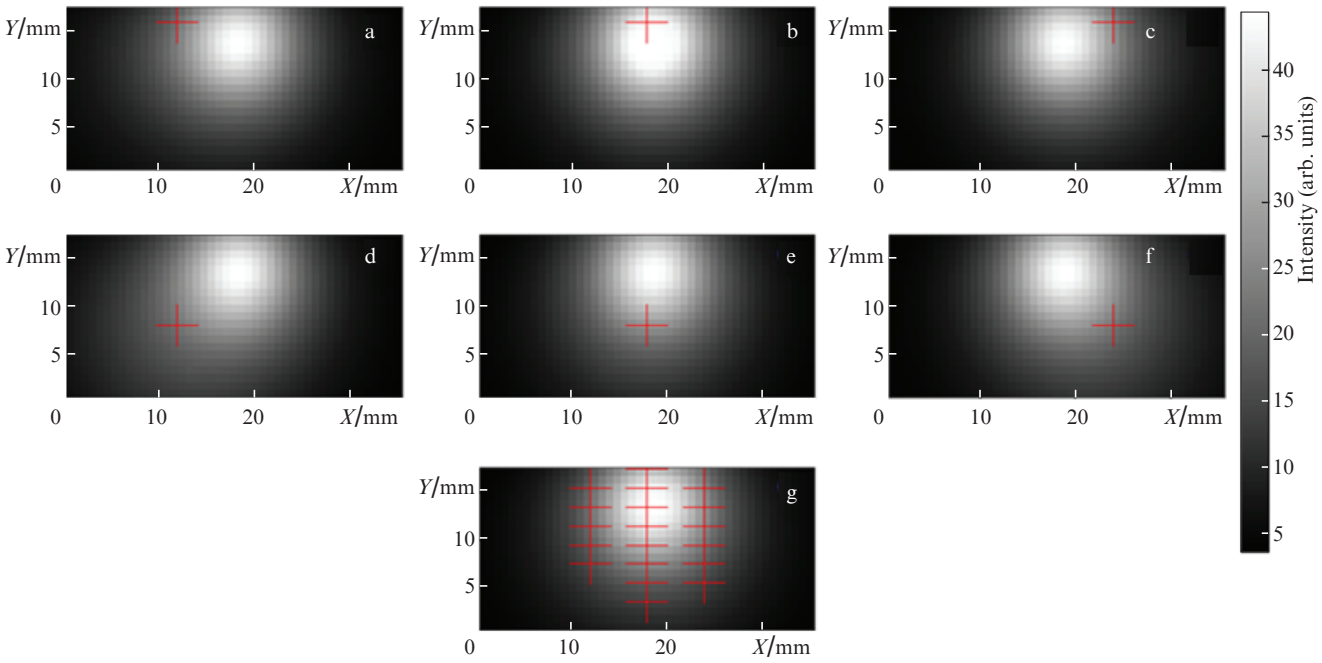

Figure 2. Examples of fluorescence images (a–f) obtained with the DFT device upon different positions of the radiation source, indicated by the '+' sign. Image (g) is averaged over 19 original fluorescence images.

The maximum (S_{max}) and minimum (S_{min}) eigenvalues of the obtained matrix $\boldsymbol{A}$ are as follows: $S_{max}(\boldsymbol{A}) \approx 1.4$ and $S_{min}(\boldsymbol{A}) < 10^{-21}$, which corresponds to the condition number of the system $S_{max}(\boldsymbol{A})/S_{min}(\boldsymbol{A}) \sim 10^{21}$. It is known that for such a value of the condition number, the standard methods for solving a system of linear equations in which there are no regularisation procedures do not allow an adequate solution to the system.

Figure 3 shows the results of reconstructing the spatial distribution of the fluorophore in the XY and XZ planes. Dashed circles indicate the true boundaries of fluorescent inclusions. Table 1 shows the numerical characteristics of the reconstruction results: the blurring of the fluorescent inclusion in two planes relative to the original size and the reconstruction time.

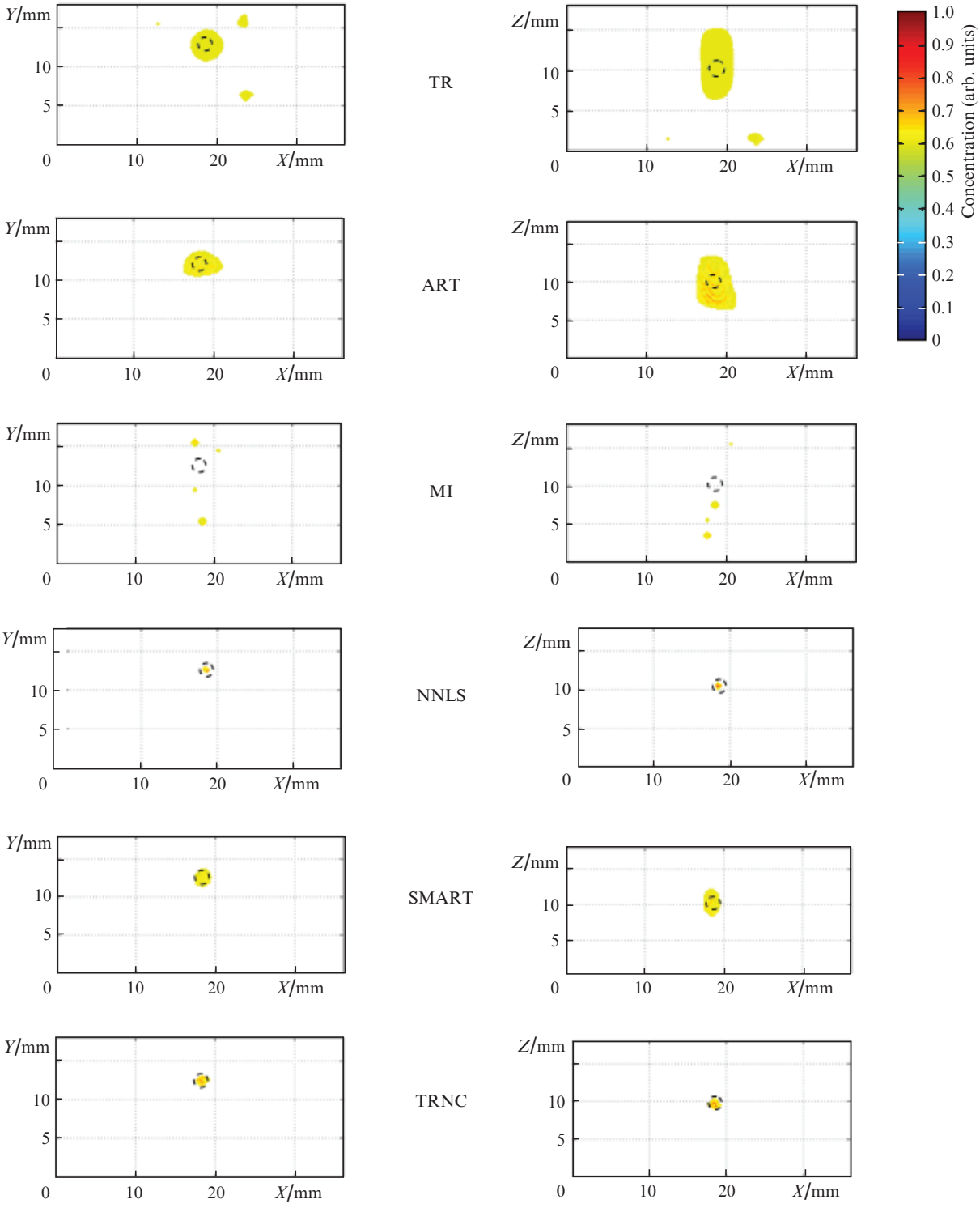

Figure 3. (Colour online) Results of three-dimensional reconstruction of a spherical fluorescent object in a biological tissue phantom in the XY and XZ planes by various methods. The dashed circles indicate the true boundaries of the fluorescent inclusion, the colour-coded map represents the distribution of the fluorophore concentration normalised to the maximum.

As can be seen from Fig. 3 and Table 1, the MI method does not allow correct reconstruction of the fluorophore distribution due to the lack of regularisation procedures. The ART and TR methods, using regularisation, reconstruct the distribution of the fluorophore correctly, but significantly, by a factor of 2–4, blur its original distribution, which is apparently due to the peculiarities of taking into account the nonnegativity conditions, namely, artificial zeroing of negative components of the solution vector at each iteration. The SMART method made it possible to obtain a distribution close to the initial one; however, due to the slow convergence of the iterative procedure, an increase in the number of iterations does not provide an improvement in the quality of reconstruction.

Table 1. The sizes of the reconstructed fluorophore distribution in comparison with the original distribution, as well as the reconstruction time for each algorithm.

Reconstruction method	Dimension in XY plane/mm	Dimension in XZ plane/mm	Reconstruction time/s
TR	4.0	9.0	300
MI	–	–	250
ART	4.0	6.7	2500
SMART	2.0	3.5	240
NNLS	1.0	1.0	500
TRNC	2.0	2.0	320

Note. The original distribution in the XY and XZ planes is 2.0 mm.

Using the NNLS method, only the position of the object centre was accurately reconstructed, but not its size, which is associated with incorrect consideration of the nonnegativity conditions, namely, the artificial zeroing of the negative components of the solution vector and the removal of the corresponding column of the system matrix at each iteration.

The developed TRNC method demonstrated the best result of reconstruction in determining both the localisation of the fluorescent inclusion and its size. This method is iterative, but each iteration is based on the results obtained by the direct MI method. Thus, the high accuracy of TRNC is provided by Tikhonov regularisation, and the nonnegativity condition is provided by an iterative procedure, which reduces errors in reconstruction compared to other methods.

Note that the reconstructed distribution of the fluorophore concentration, like the original distribution, has a spherical shape. If the object is not spherical, its true shape will be reconstructed in the presence of a sufficiently large number of projections. The results of the corresponding numerical experiments with the initial distribution of the 'shelf' type are described in Ref. [28].

3.3. Investigation of the stability of reconstruction algorithms

Figures 4 and 5 show the results of the reconstruction of a biological tissue phantom using various algorithms with a perturbed right-hand side of Eqn (5).

As can be seen from Fig. 4, using the TRNC algorithm, the shape of the fluorescent inclusion is reconstructed correctly even at large relative perturbations; however, the centre of the object is significantly displaced even at perturbations $\delta p > 0.25$. This phenomenon can be explained by the fact that the position of the object in depth is reconstructed, first of all, due to the projections obtained when the probing source is located far from the fluorescent object. However, the magnitude of the fluorescent signal in such projections is small, which means that the added noise will affect it much more than the signal obtained when the radiation source is located near the fluorescent object.

As can be seen from Fig. 5, of all reconstruction methods, only the NNLS algorithm made it possible to reconstruct correctly the original distribution of the fluorophore at $\delta p = 0.15$. This is because in NNLS, at each iteration, as in the TRNC algorithm, a system is formed and its exact solution is determined. The iterative methods ART and SMART did not allow obtaining correct solutions in the presence of even small perturbations in the right-hand side of Eqn (5), which is due

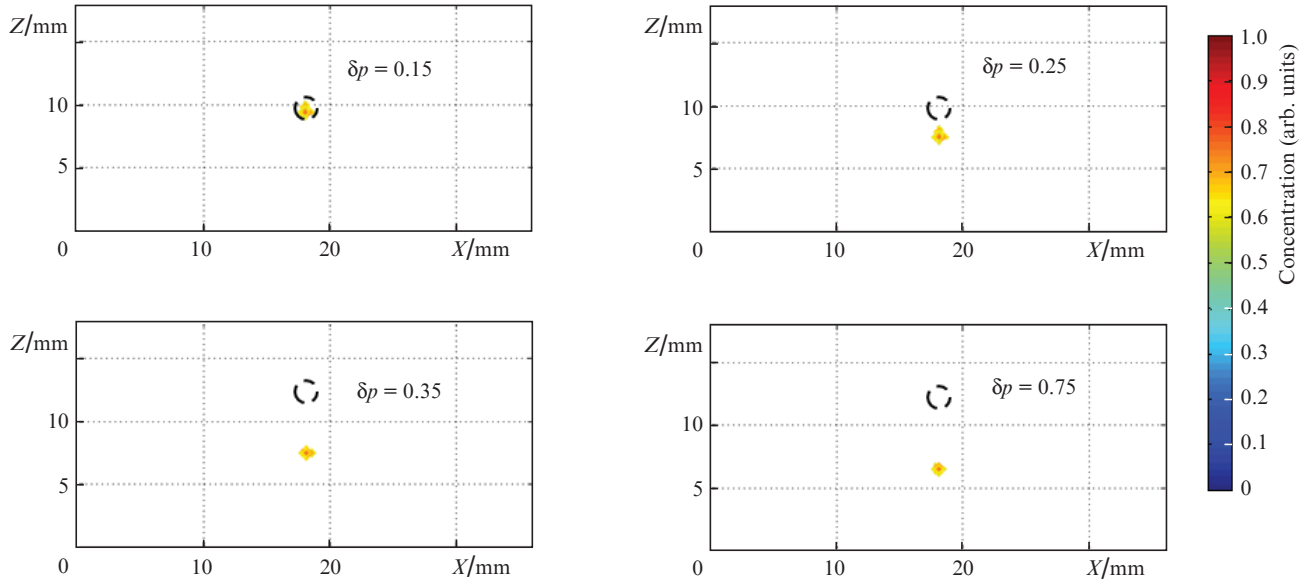

Figure 4. (Colour online) Results of three-dimensional reconstruction of a spherical fluorescent object in a biological tissue phantom in the XZ plane by the TRNC method under various relative perturbations δp. The dashed circles indicate the true boundaries of the fluorescent inclusion, the distribution of the fluorophore concentration normalised to the maximum is represented by the colour-coded map.

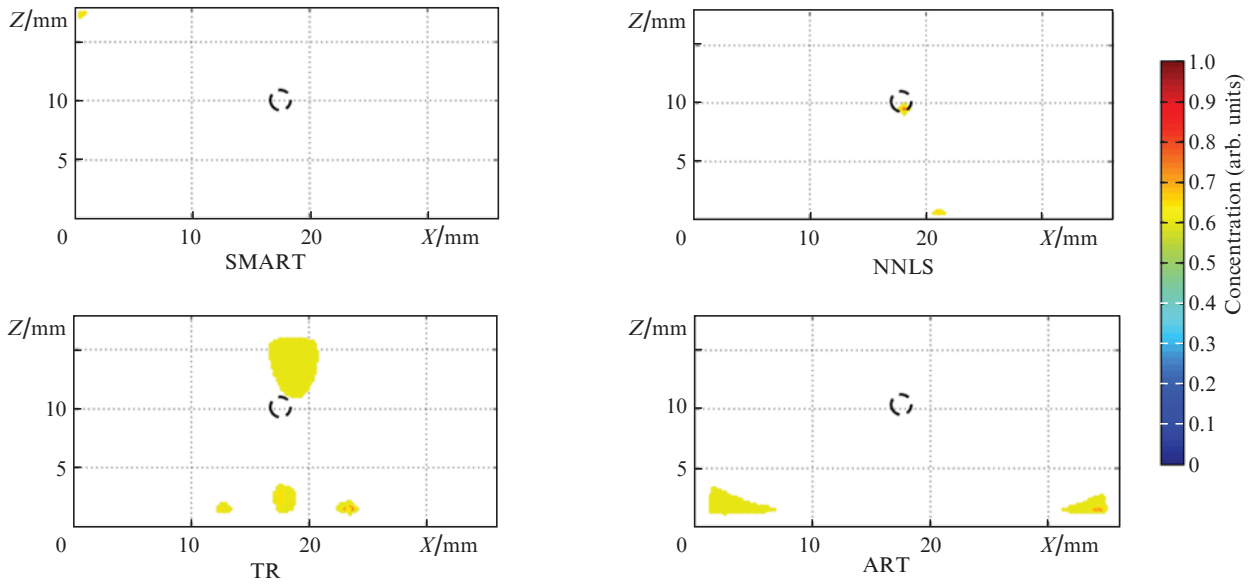

Figure 5. (Colour online) Results of three-dimensional reconstruction of a spherical fluorescent object in a biological tissue phantom in the *XZ* plane using the SMART, NNLS, TR, and ART methods at relative perturbations $\delta p = 0.15$. The dashed circles indicate the true boundaries of the fluorescent inclusion, the distribution of the fluorophore concentration normalised to the maximum is represented by the colour-coded map.

to the low convergence rate of these methods. As noted in Section 2.5, the iterative procedure of the algorithms stops when the average relative difference of adjacent iterations of the solution vector becomes less than 10^{-3}. Decreasing this threshold in the ART and SMART algorithms led to an unreasonably large increase in the reconstruction time, and it was not possible to achieve a more accurate solution in a reasonable time using these methods. The TR method also did not allow correct reconstruction of the original distribution of the fluorophore at small perturbations, because the nonnegativity condition is not taken into account in this approach.

Note that this paper presents the results of the reconstruction of a rather simple model object, which is a spherical inclusion in a uniformly scattering and absorbing turbid medium in the form of a rectangular parallelepiped. Real biological tissues are significantly heterogeneous, and their surfaces have a much more complex shape. Nevertheless, errors in variations in the optical parameters of biological tissues can be interpreted as variations on the right-hand side of Eqn (5), and since the TRNC method showed the best resistance to perturbing the right-hand side of the equation, in experiments with real biological tissues the proposed algorithm will probably also behave more stable. However, this statement requires verification using the results of scanning real biological tissues

4. Conclusions

Thus, in the present work, we propose a reconstruction algorithm for the DFT based on the TR with the condition of nonnegativity of the solution vector components. A model experiment has demonstrated a more accurate reconstruction of the distribution of fluorescent inclusion and a higher stability of this algorithm with respect to perturbations in the right-hand side of the equation in comparison with the standard ART, SMART, and NNLS methods used in DFT, as well as in comparison with the traditional TR approach to solving ill-posed problems.

Acknowledgements. The work was funded by the Ministry of Science and Higher Education of the Russian Federation within the framework of the State Assignment of the Institute of Applied Physics of RAS (Project No. 0030-2021-0014). The authors are grateful to V.A. Vorob'ev for creating the electronic parts of the DFT setup, V.I. Plekhanov for creating the optical part of the DFT setup and assistance in carrying out model experiments, and M.B. Prudnikov for creating the mechanical and housing elements of the DFT setup.

References

1. Turchin I.V. *Phys. Usp.*, **59**, 487 (2016) [*Usp. Fiz. Nauk*, **186**, 550 (2016)].
2. König K.J. *Biophoton.*, **1**, 13 (2008).
3. Sigal Y.M., Zhou R., Zhuang X. *Science*, **361**, 880 (2018).
4. Nagaya T. et al. *Frontiers Oncol.*, **7**, 314 (2017).
5. Goryainov S.A. et al. *N.N. Burdenko J. Neurosurgery*, **2** (2014) [*Zh. Vopr. Neirokhirurg. im. Burdenko*, **78**, 22 (2014)].
6. Mieog J.S.D. et al. *Annals Surg. Oncol.*, **18**, 2483 (2011).
7. Shirmanova M.V. et al. *Imaging from Cells to Animals In Vivo* (Boca Raton: CRC Press, 2020) p. 325.
8. Hoffman R.M. *J. Biomed. Opt.*, **10**, 041202 (2005).
9. Zherdeva V.V. et al. *J. Biomed. Opt.*, **23**, 035002 (2018).
10. Shirmanova M.V. et al. *Biochim. Biophys. Acta*, **1850**, 1905 (2015).
11. Pogue B.W. et al. *Technol. Cancer Res. Treat.*, **3**, 15 (2004).
12. Leblond F. et al. *J. Photochem. Photobiol. B: Biology*, **98**, 77 (2010).
13. Shirmanova M.V. et al. *J. Biomed. Opt.*, **15**, 048004 (2010).
14. Kleshnin M. et al. *Photon. Lasers Medic.*, **4**, 85 (2015).
15. Ntziachristos V. *Annu. Rev. Biomed. Eng.*, **8**, 1 (2006).
16. Zhang Y. et al. *J. Biophoton.*, **11**, e201800041 (2018).
17. Angelo J.P. et al. *J. Biomed. Opt.*, **24**, 071602 (2018).
18. Ishimaru A. *Wave Propagation and Scattering in Random Media* (New York: Academic Press, 1978; Moscow: Mir, 1981).
19. Tuchin V.V. *Handbook of Optical Biomedical Diagnostics* (Washington: Spie Press, 2002).
20. Tikhonov A.N., Arsenin V.I. *Solutions of Ill-posed Problems* (Winston: Halsted Press, 1977).
21. Gorshkov A.V., Kirillin M.Y. *J. Biomed. Opt.*, **20** (8), 085002 (2015).
22. Fiks I. et al. *Radiophys. Quantum Electron.*, **54**, 197 (2011) [*Izv. Vyssh. Uchebn. Zaved., Ser. Radiofiz.*, **54**, 219 (2011)].

23. Mohajerani P., Ntziachristos V. *IEEE Trans. Med. Imag*., **35**, 381 (2015).
24. Stuker F., Ripoll J., Rudin M. *Pharmaceutics,* **3**, 229 (2011).
25. Davis S.C. et al. *Proc. Nation. Acad. Sci*., **110**, 9025 (2013).
26. Zacharakis G. et al. *Biomed. Opt. Express*, **2**, 431 (2011).
27. Kleshnin M., Turchin I. *Laser Phys. Lett.*, **10**, 075601 (2013).
28. Fiks I. *Intern. J. Comput. Meth.*, **11**, 1350071 (2014).
29. Ntziachristos V., Weissleder R. *Opt. Lett*., **26**, 893 (2001).
30. Patwardhan S.V. et al. *Opt. Express*, **13**, 2564 (2005).
31. Okawa S. et al. *Proc. SPIE*, **8088** (2011).
32. Byrne C.L. *IEEE Trans. Image Process*., **14**, 321 (2005).
33. Lawson C.L., Hanson R.J. *Solving Least Squares Problems* (N.J.: Prentice-Hall, Englewood Cliffs, 1974).
34. Hama H. et al. *Nature Neurosci*., **14**, 1481 (2011).
35. Kong L. et al. *IEEE Transact. Med. Imag.*, **67**, 2518 (2020).
36. Baikejiang R. et al. *J. Biomed. Opt*., **22**, 055001 (2017).
37. Zhang S. et al. *IEEE Transact. Med. Imag.,* **37**, 2176 (2018).
38. Meng H. et al. *IEEE Transact. Med. Imag*., **39**, 3019 (2020).
39. Turchin I.V. et al. *J. Biomed. Opt*., **13**, 041310 (2008).